ACS central science

http://pubs.acs.org/journal/acscii

Research Article

Multiparameter Longitudinal Imaging of Immune Cell Activity in Chimeric Antigen Receptor T Cell and Checkpoint Blockade Therapies

Jinghang Xie, Fadi El Rami, Kaixiang Zhou, Federico Simonetta, Zixin Chen, Xianchuang Zheng, Min Chen, Preethi B. Balakrishnan, Sheng-Yao Dai, Surya Murty, Israt S. Alam, Jeanette Baker, Robert S. Negrin, Sanjiv S. Gambhir, and Jianghong Rao*

Cite This: *ACS Cent. Sci.* 2022, 8, 590−602

Read Online

ABSTRACT: Longitudinal multimodal imaging presents unique opportunities for noninvasive surveillance and prediction of treatment response to cancer immunotherapy. In this work we first designed a novel granzyme B activated self-assembly small molecule, G-SNAT, for the assessment of cytotoxic T lymphocyte mediated cancer cell killing. G-SNAT was found to specifically detect the activity of granzyme B within the cytotoxic granules of activated T cells and engaged cancer cells *in vitro*. In lymphoma tumor-bearing mice, the retention of cyanine 5 labeled G-SNAT-Cy5 correlated to CAR T cell mediated granzyme B exocytosis and tumor eradication. In colorectal tumor-bearing transgenic mice with hematopoietic cells expressing firefly luciferase, longitudinal bioluminescence and fluorescence imaging revealed that after combination treatment of anti-PD-1 and anti-CTLA-4, the dynamics of immune cell trafficking, tumor infiltration, and cytotoxic activity predicted the therapeutic outcome before tumor shrinkage was evident. These results support further development of G-SNAT for imaging early immune response to checkpoint blockade and CAR T-cell therapy in patients and highlight the utility of multimodality imaging for improved mechanistic insights into cancer immunotherapy.

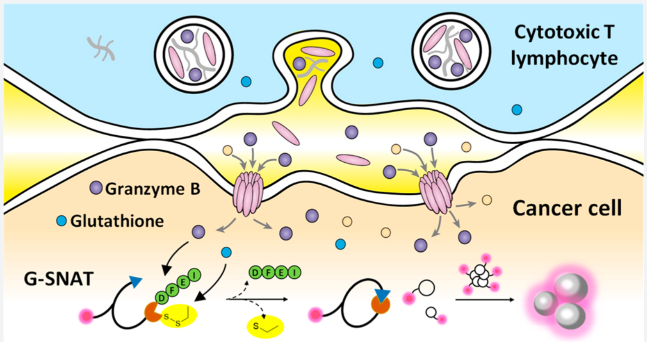

INTRODUCTION

Cancer immunotherapies, mainly immune checkpoint blockade and adoptive cell transfer (e.g., chimeric antigen receptor-CAR T-cell therapy), have significantly improved survival rates in many cancers by providing robust and sustained therapeutic effects.[1,2] Yet, many hurdles such as complex immune evasion mechanisms, dysfunction of T lymphocytes, and the immunosuppressive tumor microenvironment[3−11] limit treatment efficacy.[12,13] Additionally, life-threatening immune-related side effects are not uncommon.[14] Tremendous efforts are now being devoted to understanding and targeting these mechanisms for the development of more effective therapies with improved safety profiles. Noninvasive molecular imaging is a promising strategy for monitoring whole-body immune responses both during disease progression and upon treatment induction.[15]

Radiolabeled antibodies,[16−19] peptides,[20] or small molecules[21,22] that target surface markers or show uptake by specific immune cell populations have been extensively studied for imaging the immune response. The presence of specific tumor-infiltrating immune cells, for example, CD8+ cytotoxic T lymphocytes (CTLs), has been shown to correlate with a favorable response to checkpoint blockade therapy.[23−25] Nevertheless, several known immunotolerant mechanisms associated with the suppressive tumor microenvironment such as T cell anergy, exhaustion, or senescence may compromise the accuracy for predicting the therapeutic response solely based on the presence of cell subsets.[26,27] Alternatively, granule-mediated cytotoxicity by natural killer (NK) cells and CTLs has been explored for monitoring the immune activity responsible for tumor eradication.[28,29] Granule-mediated cytotoxicity, one of the dominant cytotoxic mechanisms used by immune effectors, involves the release of granzyme B (gzmB)-loaded granules to induce the lysis of target cells.[30] Secreted gzmB is intrinsically stable, representing an ideal biological target of cytotoxicity.[31] A number of imaging probes have been developed to study gzmB function *in*

Received: February 7, 2022
Published: May 12, 2022

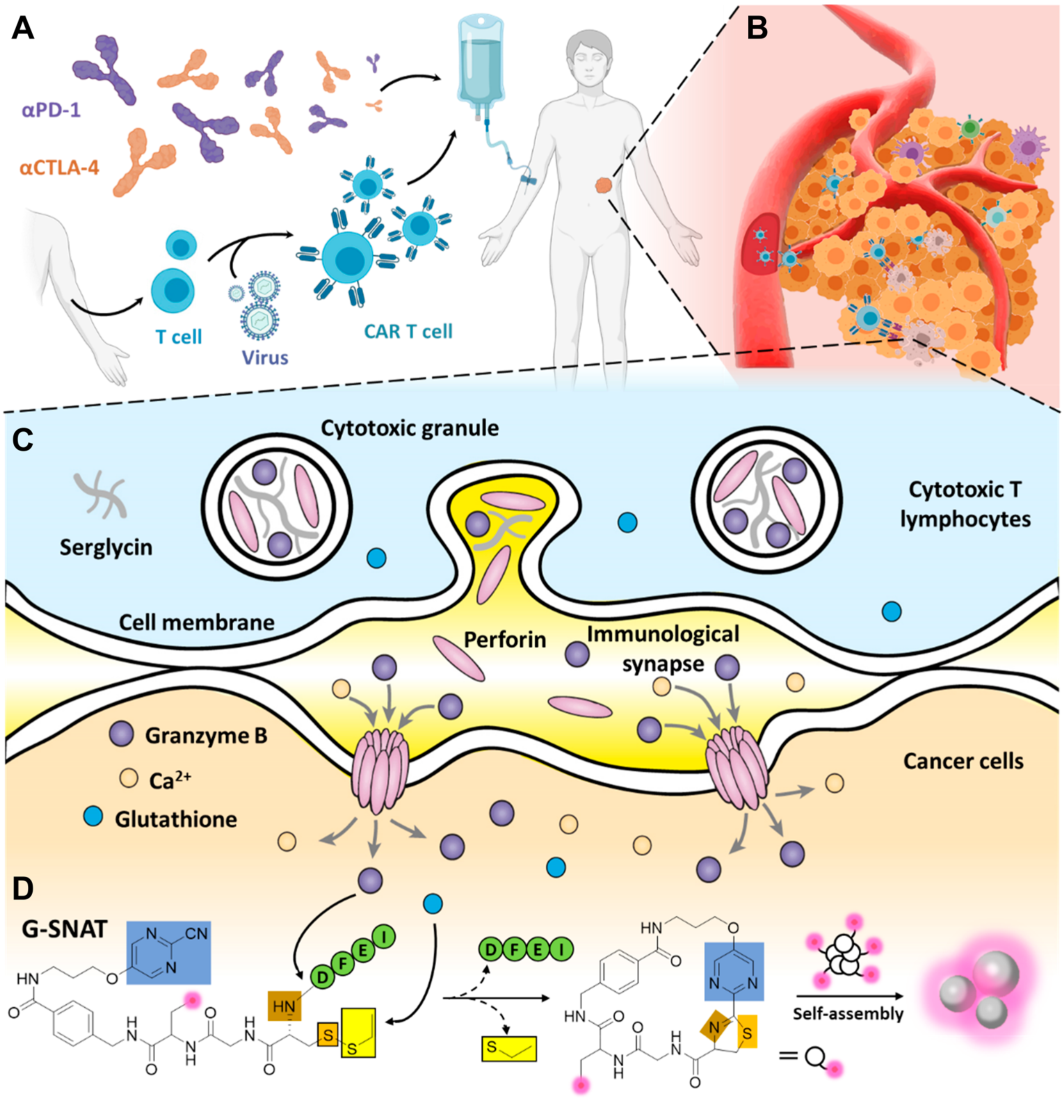

Figure 1. Mechanism of *in vivo* imaging of gzmB activity in tumors by G-SNAT. (A) Treatment of a patient with checkpoint inhibitors or CAR T cells. (B) Effector T cells (blue) can extravasate and infiltrate tumors to kill cancer cells (yellow). (C) Production of gzmB and perforin by CTLs and their delivery across an immunological synapse into cancer cells. (D) Proposed gzmB and reduction-controlled conversion of G-SNAT into G-SNAT-cyclized through the bioorthogonal intramolecular cyclization, followed by self-assembly into nanoaggregates *in situ*. Blue square, the 2-cyanopyrimidine; brown and orange, amino and thiol groups of D-cysteine, respectively; yellow, thioethyl masking group; green, the capping peptide residues; pink, fluorophore Cy5. Part of this figure was created with BioRender.com.

vitro[32,33] and image gzmB activity *in vivo*,[34−37] supporting gzmB as a useful biomarker of cytotoxic cell activation in anticancer responses.[28,38,39] However, these studies did not monitor the gzmB activity together with the immune cell trafficking and tumor infiltration. Given the highly complex and regulated nature of the immune system, sequential imaging of multiple events of immune response in the same animals can help reveal the complicated spatiotemporal dynamics of immune activity and uncover immune evasion mechanisms.

In this study, we first developed a sensitive fluorescent imaging probe for noninvasive surveillance of gzmB function. This probe, termed a gzmB sensitive nanoaggregation tracer (G-SNAT-Cy5), was designed based on the TESLA (target-enabled *in situ* ligand aggregation), a versatile probe platform built on the bioorthogonal condensation reaction between an aromatic nitrile and cysteine.[40−42] The TESLA platform has been demonstrated for the development of small-molecule imaging probes for multimodality imaging of proteolytic enzyme activity.[43−49] A TELSA probe is made of a scaffold containing an aromatic nitrile such as cyanoquinoline or pyrimidinecarbonitrile and a cysteine whose amino group is conjugated to a caging moiety—a peptide substrate of gzmB in the case of G-SNAT. Upon uncaging by the target, for example, gzmB, the cysteine group will react with the aromatic nitrile intermolecularly or intramolecularly to form macrocyclic products. Promoted by hydrophobic and $\pi-\pi$ interactions, these products will form molecular aggregates at the nano scale, resulting in preferential retention at the target site. A cyanine 5 fluorophore (Cy5) labeled G-SNAT-Cy5 probe was validated for imaging the activity of gzmB both *in vitro* and in clinically relevant mouse models of CAR T-cell and checkpoint blockade therapies. We discovered that gzmB could maintain partial hydrolytic activity under acidic conditions within cytotoxic granules. G-SNAT-Cy5 not only detected gzmB activity within the CTLs but also reported the CAR T cell mediated cytotoxicity *in vivo*, a major advantage over

https://doi.org/10.1021/acscentsci.2c00142
ACS Cent. Sci. 2022, 8, 590−602

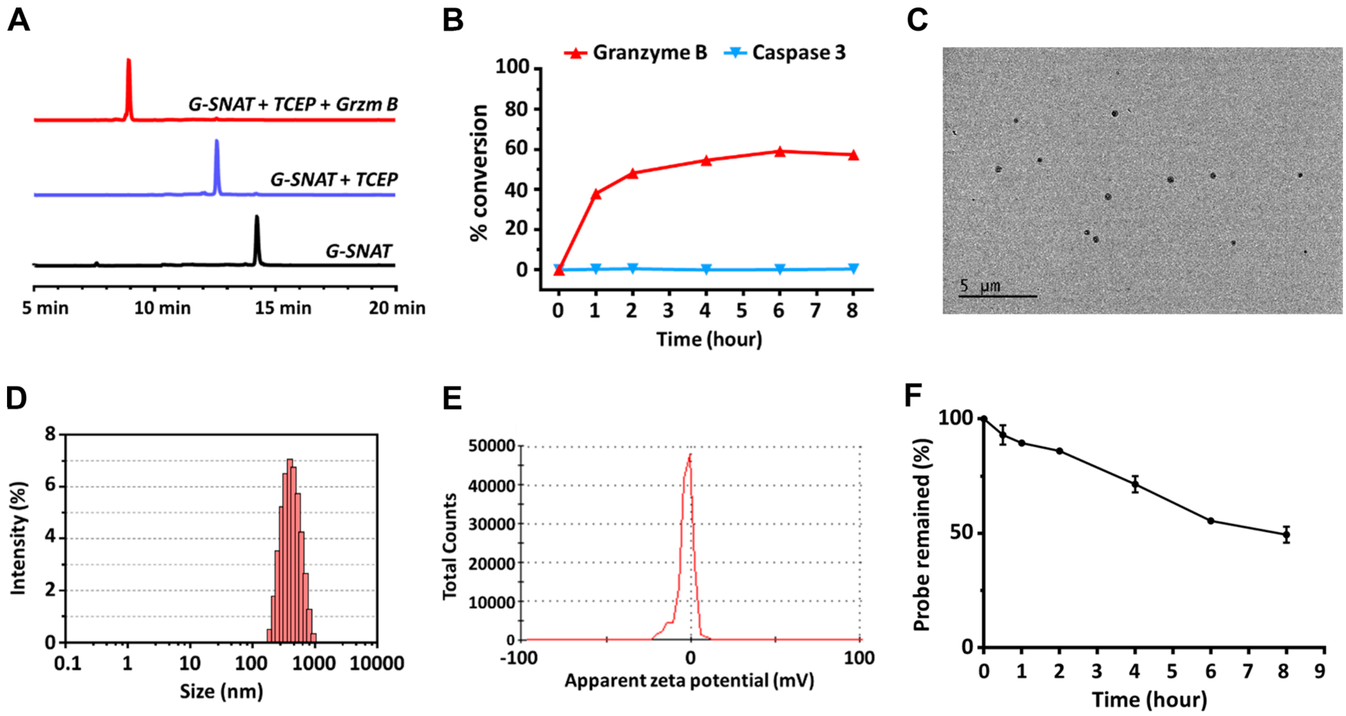

Figure 2. *In vitro* characterization of the G-SNAT probes. (A) HPLC traces of G-SNAT in gzmB assay buffer (black, T_R = 14.2 min) and the incubation of G-SNAT (10 μM) with TCEP (blue, T_R = 12.8 min) and recombinant mouse gzmB (1 μg/mL) overnight at 37 °C (red, T_R = 8.9 min). (B) The enzymatic reaction kinetics and specificity studies by longitudinal monitoring of the percentage conversion of G-SNAT (10 μM) into G-SNAT-cyclized after incubation with equal amounts (100 U) of recombinant mouse gzmB (0.05 μg/mL) and human caspase-3. (C) TEM image of nanoaggregates after the incubation of G-SNAT (100 μM) with recombinant mouse gzmB (1 μg/mL) overnight at 37 °C in assay buffer. (D) DLS analysis of diluted (2×) G-SNAT-cyclized (50 μM) showing the distribution of particle sizes. (E) Measurement of the zeta potential of G-SNAT-cyclized. (F) Analysis of the stability of G-SNAT in mouse serum by HPLC. The percentage of probe remaining after the incubation of 100 μM of G-SNAT-Cy5 in mouse serum at 37 °C for indicated times was obtained by calculating the percentage of the peak area (mAU*min) of the probe on the corresponding HPLC trace; error bars (S.D.) were calculated from two separate experiments.

conventional T cell-tracking techniques. Employing longitudinal bioluminescence imaging of transgenic mice with hematopoietic cells engineered to stably express firefly luciferase, we simultaneously determined the immune cell trafficking and tumor infiltration in response to immunotherapies. This combined imaging of immunological events revealed distinct whole-body patterns of immune cell migration and associated cytotoxicity among checkpoint inhibitors treated responder, nonresponder, and untreated groups and allowed earlier and reliable prediction of immunotherapeutic outcomes. These results highlight the value of multimodal longitudinal imaging for monitoring complex immune dynamics and their orchestration in response to immunotherapies.

■ RESULTS

Design of gzmB-Sensitive Nanoaggregation Probes. In effective CAR T-cell or checkpoint blockade therapies (Figure 1A), CTLs extravasate, infiltrate, and engage cancer cells to establish immunological synapses which enable rapid, polarized release of cytotoxic granules containing effector proteins perforin and gzmB at the synaptic cleft (Figure 1B). Perforin, as named, directly perforates the target-cell plasma membrane and oligomerizes in a calcium-dependent manner into a conduit which allows the passive diffusion of gzmB to trigger programed cell death (Figure 1C). GzmB is a serine protease that cleaves an IEFD (Ile-Glu-Phe-Asp) peptide motif (preferred substrate in mice) to activate downstream caspase signaling and trigger DNA fragmentation and apoptosis (Figure 1C).[50−53] This unique mechanism in the cytotoxic immune response provides efficient delivery of active gzmB into target cells, in addition to an endocytosis-dependent mechanism that has also been proposed.[54,55]

Based on our highly modular TESLA, G-SNAT was designed (Supporting Information Figures S1 and S2) to uniquely enable the projection of specific catalytic activity of gzmB during immune response assessment to retained molecular aggregates. As illustrated in Figure 1D, G-SNAT contains (1) a 2-cyanopyrimidine group (blue), (2) a cysteine residue coupled to the IEFD substrate (green) at the amino group (brown) with a disulfide bond at the mercapto group (orange), and (3) a propargylglycine residue between pyrimidine and the cysteine for labeling with a fluorophore, radioisotope, or other contrast agents (pink). After hydrolysis and cleavage of IEFD by gzmB as well as the reduction of the disulfide bond by intracellular glutathione (GSH), the product cyclizes intramolecularly into macrocyclics which are rigid, hydrophobic, and susceptible to intermolecular interactions that trigger nanoaggregation *in situ*. For studies *in vitro*, both a Cy5 preconjugated G-SNAT-Cy5 probe (Supporting Information Figure S2) and post cell culture click reaction at the propargylglycine alkyne handle with an azido Cy5 were applied for pinpointing the aggregated G-SNAT in cells.

Macrocyclization and Nanoaggregation of G-SNAT *In Vitro*. Incubation of G-SNAT with recombinant mouse gzmB enzyme (1 μg/mL) and tris(2-carboxyethyl)phosphine (TCEP, 2 mM) to mimic the intracellular reducing environment at 37 °C overnight enabled the macrocyclization of G-SNAT (10 μM; retention time, T_R = 14.2 min) to give G-

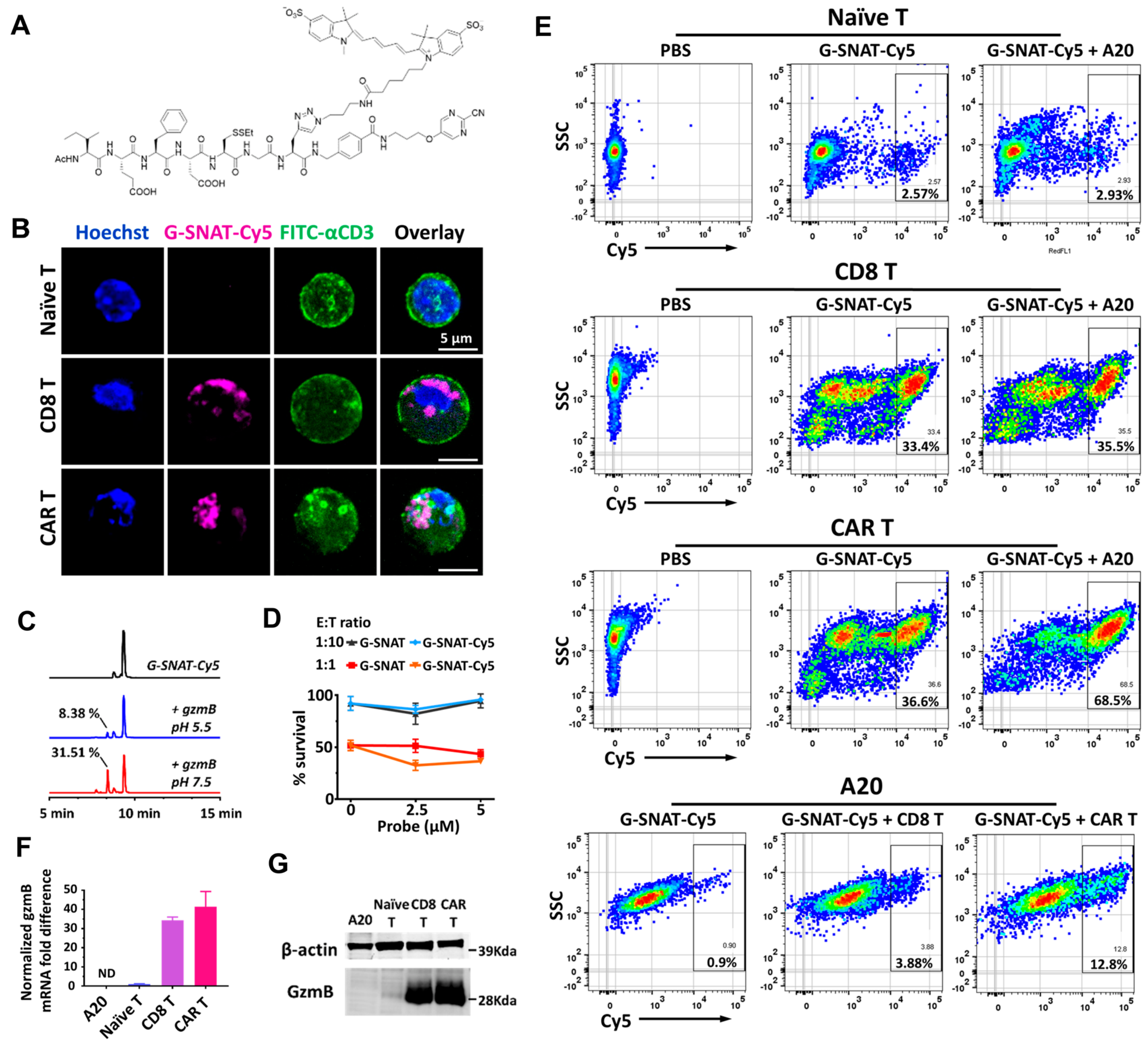

Figure 3. GzmB activity in naive CD8+ T, activated untransduced CD8+ T, CD19-28ζ CAR T, and A20 cancer cells. (A) Structure of G-SNAT-Cy5. (B) Microscopic imaging of T cells incubated with G-SNAT-Cy5 (5 μM) for 2.5 h and then stained with Hoechst (blue, Ex390/Em440) and FITC conjugated CD3 antibody (green, Ex488/Em520). Magenta (Ex650/Em670) represents retained G-SNAT-Cy5. (C) HPLC traces of G-SNAT-Cy5 (black) and incubation with gzmB (0.05 μg/mL) in MES buffer (pH 5.5, blue) or assay buffer (pH 7.5, red) at 37 °C for 2 h; 8.38% and 31.51% indicate the percent conversion relative to the G-SNAT-Cy5 peak as calculated from the peak areas (mAU*min). (D) G-SNAT or G-SNAT-Cy5 treatment (0, 2.5, and 5 μM) showed no impact on the cytotoxic function of CD19-28ζ CAR T cells against A20^{Luc+} cells. Error bars (S.D.) are calculated from triplicated experiments. (E) Flow cytometry analysis of PBS or G-SNAT-Cy5 treated naive CD8+ T, activated untransduced CD8+ T and CAR T cells with or without A20 cells, and A20 cells incubated with or without activated untransduced CD8+ T and CAR T cells. 10 000 cells were analyzed. T cells were incubated with A20 cancer cells at a 1:1 ratio for 2.5 h. The gates indicate high G-SNAT-Cy5 retention in cells. (F) Quantitative RT-PCR analysis of gzmB mRNA. ND: nondetectable. (G) Western blot analysis of gzmB in cell lysate (25 μg).

SNAT-cyclized (T_R = 8.8 min), as shown in high-performance liquid chromatography (HPLC) and confirmed by mass spectrometry (Figure 2A). Since IEFD has been reported to be a preferred substrate of mouse gzmB and its specificity has been validated,[35,56] we conducted a kinetic study with caspase 3 as a control, which was believed to share a pool of substrates with gzmB like the nuclear mitotic apparatus protein (NuMA, Val-Leu-Gly-Asp) and DNA-dependent protein kinase catalytic subunit (DNA-PKcs, Asp-Glu-Val-Asp).[57] It was shown that gzmB, not caspase 3, activated G-SNAT (10 μM) and converted it to cyclized product (Figure 2B and Supporting Information Figure S3). The assembled nanoaggregation was imaged with transmission electron microscopy (TEM), and the size distribution was acquired by dynamic light scattering (DLS) (Figure 2C and D). The average diameter of the aggregated nanostructures was 396 nm, ranging from 190 to 955 nm. No DLS signal could be detected when G-SNAT remained uncleaved by gzmB. The nanoaggregates were found nearly neutral by zeta potential analysis (Figure 2E). Together, these results demonstrate that gzmB specifically hydrolyzes IEFD and induces macrocyclization of the products leading to intermolecular interaction and nanoaggregation. The stability

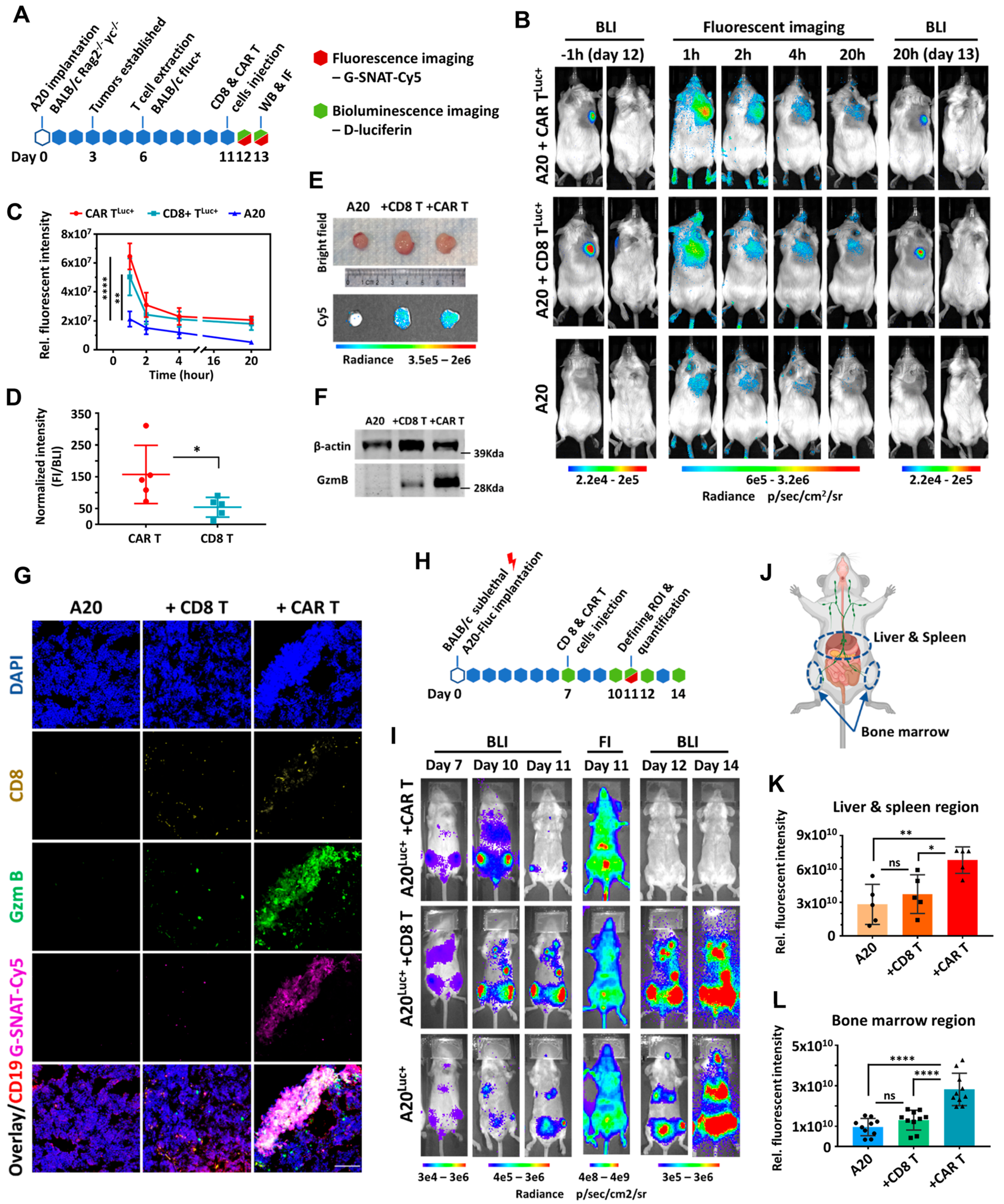

Figure 4. Multimodal optical imaging with G-SNAT-Cy5 and D-luciferin predicts lympoid tumor response to CAR T-cell therapy. (A) Illustration of the workflow to generate the subcutaneous A20 lymphoid tumor/CD19-28ζ CAR T^{Luc+} cell therapy model and imaging study with D-luciferin and G-SNAT-Cy5. (B) Longitudinal bright-field, bioluminescence, and fluorescence imaging with D-luciferin and G-SNAT-Cy5 (5 nmol, Ex640/Em690) of A20 implanted (bottom), activated untransduced CD8+ T^{Luc+} (middle), or CAR T^{Luc+} cells (top) treated tumor-bearing mice. T cells were injected at the tumor site. Representative mice are shown here while full panels are shown in Supporting Information Figures S15 and S16. (C) A comparison of the relative fluorescence intensity acquired by defining ROIs on PBS, untransduced activated CD8+ T^{Luc+}, or CAR T^{Luc+} cells treated A20 tumors at 1, 2, 4, and 20 h postinjection. $^{**}p < 0.0021$-A20 vs CD8+ T^{Luc+} cells treated; $^{****}p < 0.0001$-A20 vs CAR T^{Luc+} cells treated. (D) A comparison of the normalized intensity (FI, fluorescence imaging/BLI, bioluminescence imaging) of untransduced activated CD8+

https://doi.org/10.1021/acscentsci.2c00142
ACS Cent. Sci. 2022, 8, 590−602

Figure 4. continued

T^{Luc+} and CAR T^{Luc+} cells treated A20 tumors at 1 h postinjection. *$p < 0.0332$. (E) Bright-field and fluorescence imaging of PBS, CD8+ T^{Luc+}, or CAR T^{Luc+} cells treated tumors at day 13. Major ruler unit is cm. (F) Western blot analysis of gzmB in tumor lysate (50 μg) from (E). (G) Immunofluorescence staining analysis of the tumors in (E). (H) Illustration of the workflow to generate the systemic lymphoma/CD19-28ζ CAR T^{Luc+} cell therapy model and imaging study with D-luciferin and G-SNAT-Cy5. (I) Longitudinal bright-field, bioluminescence, and fluorescence imaging with D-luciferin and G-SNAT-Cy5 (5 nmol, Ex650/Em670) of $A20^{Luc+}$ implanted (bottom), activated untransduced CD8+ T (middle), or CAR T cells (top) treated tumor-bearing mice. Representative mice are shown here while full panels are shown in Supporting Information Figure S17. (J) Cartoon illustrating the defined ROI on liver and spleen (middle circle) and bone marrow (lower two circles) regions to estimate the fluorescence intensity. (K) A comparison of the relative fluorescence intensity acquired by defining the ROI on liver and spleen regions of $A20^{Luc+}$, activated untransduced CD8+, or CAR T cells treated tumor-bearing mice. Error bars represent S.D. *$p < 0.0332$; **$p < 0.0021$, ns: not significant. (L) A comparison of the relative fluorescence intensity acquired by defining the ROI on bone marrow regions of $A20^{Luc+}$, activated untransduced CD8+, or CAR T cells treated tumor-bearing mice. Error bars represent S.D. ****$p < 0.0001$.

of G-SNAT-Cy5 in mouse serum was evaluated by HPLC and indicated a half-life of approximately 8 h (Figure 2F and Supporting Information Figure S4), which is sufficiently stable to capture serial immunological synapse activity that usually lasts less than 15 min each.

G-SNAT-Cy5 Imaging Report gzmB Activity in Cytotoxic T Cells and CAR T Cell Engaged Cancer Cells. To examine whether G-SNAT-Cy5 (Figure 3A) could report gzmB activity in cytotoxic T cells, we isolated CD8+ T cells from BALB/c mice, activated them with anti-CD3/CD28-coated beads, and divided these cells into two groups: one underwent retroviral transduction to generate CD19-28ζ CAR-T cells, as previously described,[58] while the other group was left untransduced. Nonactivated naive T cells ($CD44^{low}CD62L^{high}$) were prepared as the control (Supporting Information Figure S5). After 2.5 h of incubation with G-SNAT-Cy5 (5 μM), confocal microscopic imaging revealed fluorescence in both activated untransduced CD8+ and CAR T cells but not in naive T cells (Figure 3B and Supporting Information Movies S1, S2, and S3). After its synthesis, gzmB was packaged and activated in lytic granules to prevent self-killing and to facilitate trafficking to the immunological synapse.[59] The images were consistent with such granular sequestration of intracellular active gzmB and suggested the retention of *in situ* aggregated G-SNAT-Cy5 (Supporting Information Figure S6). Intriguingly, gzmB-packed granules displayed a denser fluorescent cluster in CAR T versus untransduced activated CD8+ T cells (Figure 3B). This might concur with faster lytic granule recruitment to nonclassical CAR T cell immune synapses described by Davenport et al.,[60] which was characterized by a lack of Lck clustering at small immunological synapses, in contrast to wild type T cells with the Lck-rich, large immunological synapses. Incubation of activated untransduced CD8+ T cells at 4 °C significantly attenuated G-SNAT-Cy5 uptake (Supporting Information Figure S7), suggesting an energy-dependent endocytic process rather than passive membrane diffusion. To validate that gzmB retained enzymatic activity in granules, we tested recombinant mouse gzmB under acidic (pH 5.5) conditions and found that the enzyme maintained about 26.6% and 24.3% of its activity at pH 5.5 after 2 and 4 h incubation with G-SNAT-Cy5 at 37 °C, respectively (Figure 3C and Supporting Information Figure 8). Bioluminescence assay with BALB/c B cell lymphoma line derived A20 cells expressing firefly luciferase ($A20^{Luc+}$) confirmed that the cytotoxic function of these CAR T cells was not affected by overnight incubation with G-SNAT or G-SNAT-Cy5 (Figure 3D and Supporting Information Figure S9). Further viability study showed that both G-SNAT and G-SNAT-Cy5 were well tolerated by $A20^{Luc+}$, CD8+ T, and CAR T cells (Supporting Information Figure S10). Collectively, these results suggest activation and retention of G-SNAT-Cy5 by gzmB in the granules of cytotoxic T cells in a bioorthogonal manner.

Next, we investigated whether G-SNAT-Cy5 could differentiate antigen specific cytotoxic killing by CAR T cells from activated untransduced CD8+ T cells in two established CAR T-cell therapy models *in vitro*: CD19−28ζ CAR T cells cocultured with A20 cells naturally expressing CD19 and GD2-4-1BBζ CAR T cells (transduced from total T cells) cocultured with SB28 murine glioblastoma cells engineered to stably express red fluorescent protein (RFP) and mouse GD2 (SB28-RFP/GD2). Both CAR T cells were freshly prepared and maintained according to previously reported protocols.[58,61] Naive, activated untransduced CD8+ and CD19-28ζ CAR T cells were first incubated with A20 cells in suspension at a 1:1 ratio (effector:target) in the presence of G-SNAT-Cy5 (5 μM) for 2.5 h. The live cells were analyzed by flow cytometry. Cancer and T cells were gated (Supporting Information Figure S11), and their mean fluorescence intensity of Cy5 (MFI-Cy5) was individually quantified. As shown in both 2D plots (side scatter-*y*-axis; MFI-Cy5-*x*-axis) (Figure 3E) and statistical analysis (Supporting Information Figure S12), exposure to cognate antigens greatly enhanced the G-SNAT-Cy5 activation in CAR T cells. A20 cells under CAR T cell-mediated cytotoxic killing had also elevated G-SNAT-Cy5 retention, although a small number of nonspecific killings were observed with untransduced CD8+ T cells (Supporting Information Figure S12A). Without an antigen, CAR T cells had also higher G-SNAT-Cy5 retention than activated untransduced CD8+ T cells (Supporting Information Figure S12B). We analyzed the expression of gzmB in these cancer and T cells at both transcriptional (Figure 3F) and protein levels (Figure 3G). GzmB was robustly expressed in activated CD8+ and CAR T cells, negligible in naive T cells, and completely nondetectable in A20 cells. CD19-28ζ CAR transduction allowed higher gzmB expression in CAR T cells, which correlated to the higher activation of G-SNAT-Cy5. Inclusion of a competitive gzmB inhibitor (Ac-IETD-CHO)[62] significantly compromised the retention of G-SNAT-Cy5 in CAR T cells (Supporting Information Figure S12C). To rule out that Cy5 fluorophore dominated the uptake and nanoaggregation of G-SNAT-Cy5, we repeated the study in GD2-4-1BBζ CAR T-cell treated SB28-RFP/GD2 cells with a postclick imaging strategy as previously described (Supporting Information Figure S13).[47] A caspase-3 sensitive nanoaggregation probe C-SNAT4 developed previously[42] was included to show apoptosis triggered by cytotoxic killing. Consistent with the prelabeled probe, G-SNAT was highly activated and retained in CAR T and

https://doi.org/10.1021/acscentsci.2c00142
ACS Cent. Sci. 2022, 8, 590−602

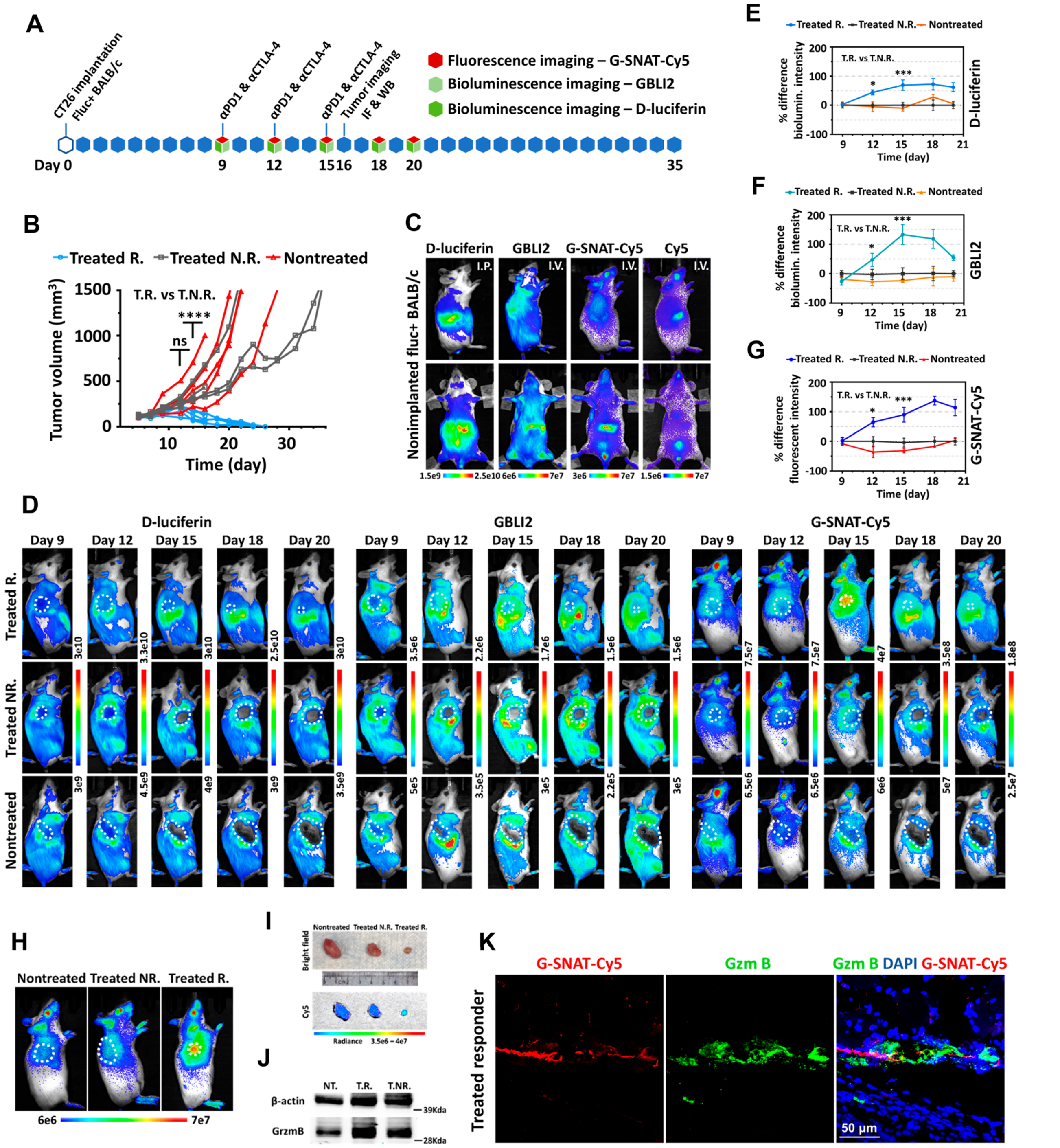

Figure 5. Imaging with G-SNAT-Cy5, GBLI2, and D-luciferin to predict colorectal tumor reponse to checkpoint blockade therapy. (A) Illustration of the workflow to generate the subcutaneous CT26 colorectal tumor in Fluc+ BALB/c mice treated with anti-PD-1 and anti-CTLA-4 and imaging studies with G-SNAT-Cy5, GBLI2, and D-luciferin. (B) Growth of the tumors in treated responder (T.R.), treated nonresponder (T.N.R.), and nontreated cohorts. Three of the mice were sacrificed at day 16 for *ex vivo* analysis. Day 12 ns: not significant, day 14 $^{****}p < 0.0001$. (C) Bright-field, bioluminescence, and fluorescence imaging of healthy Fluc+ BALB/c mice showing the baseline uptake and distribution of D-luciferin (3 mg, i.p), GBLI2 (200 μg, i.v. retro orbital), G-SNAT-Cy5 (5 nmol, i.v. retro orbital, Ex640/Em690), and Cy5 (5 nmol, i.v. retro orbital, Ex640/Em690). (D) Longitudinal bioluminescence imaging with D-luciferin (3 mg, i.p.), GBLI2 (200 μg, i.v. retro orbital), and fluorescence imaging with G-SNAT-Cy5 (5 nmol, i.v. retro orbital) of nontreated (bottom), treated nonresponder (middle), and responder (top) groups. White circles indicate tumors. Representative mice from each group are shown. (E), (F), and (G) Relative bioluminescent and fluorescent intensity of tumors at day 9, 12, 15, 18, and 20 were quantified by defining ROIs on tumors. The percent differences of bioluminescence and fluorescence intensity among treated responder, treated nonresponder, and nontreated over the course of imaging are plotted using the treated nonresponder as the baseline; $n = 5$ for Treated R., $n = 4$ for Treated N.R., and $n = 5$ for Nontreated. $^{*}p < 0.0332$, $^{***}p < 0.0002$. Error bars represent S.D. (H) Bright-field and G-SNAT-Cy5 fluorescence imaging of the mice at day 16 before euthanasia and tumor collection. White circles indicate tumors. (I) Bright-field and fluorescence imaging of tumors collected from (H). Major ruler unit is cm. (J) Western blot analysis of gzmB from (I). 50 μg of tumor lysate was loaded for analysis. (K) Immunofluorescent staining analysis of treated responded tumor from (I).

https://doi.org/10.1021/acscentsci.2c00142
ACS Cent. Sci. 2022, 8, 590−602

engaged cancer cells after 2.5 h incubation at a 2:1 ratio. Additional caspase-3 imaging pinpointed the apoptotic cells without nonspecific detection of gzmB (Supporting Information Figure S14). Together, these results demonstrate that G-SNAT probes can image the activity of gzmB from CTLs during immunotherapy.

Bioluminescence and G-SNAT-Cy5 Fluorescence Imaging Reveal gzmB-Mediated Cytotoxic Activity in CAR T Cells Treated Lymphoma Models. To assess the ability of G-SNAT-Cy5 to report gzmB activity during CAR T cell mediated cytotoxicity *in vivo*, we tested a gzmB-releasing model by subcutaneously (s.c.) implanting A20 cells into the upper right flank of BALB/c Rag2$^{-/-}\gamma$c$^{-/-}$ mice and treated them with CD19-28ζ CAR T^{Luc+} cells (Figure 4A). These CAR-T^{Luc+} cells were generated by retroviral transduction of activated CD8+ T^{Luc+} cells from transgenic Fluc+ BALB/c mice with hematopoietic cells engineered to stably express firefly luciferase.[63] When the tumor volume reached ~300 mm^3, 6 × 10^6 activated untransduced CD8+ or equivalent CAR T^{Luc+} cells (~70% transduction efficacy) were intratumorally injected. The abundance, viability, and distribution of these T cells were monitored by bioluminescence imaging with standard intraperitoneal (i.p.) administration of D-luciferin (3 mg) at 24 h (day 12 post A20 implantation) and 48 h (day 13) post T cell injection. Associated gzmB activity was longitudinally imaged at 1, 2, 4, and 20 h post tail vein administration of G-SNAT-Cy5 (5 nmol) at day 12. At day 13, the tumors were removed, imaged, and analyzed by western blot and immunofluorescence staining after another round of G-SNAT-Cy5 imaging (Figure 4A). As shown in Figure 4B, both activated untransduced CD8+ and CAR T^{Luc+} cells maintained viability 24 h post intratumoral injection, although a faster decay of CAR T^{Luc+} cells within the semisolid tumor microenvironment was noticed (Supporting Information Figure S15). The regions of interest (ROIs) on tumors were defined to quantify both bioluminescent and fluorescent intensity (Supporting Information Figure S16). The highest fluorescent intensity of G-SNAT-Cy5 was observed at 1 h postinjection in CAR T^{Luc+} cells treated tumors which was on average 3.1-fold of the PBS and 1.3-fold of the activated untransduced CD8+ T^{Luc+} cells treated tumors (Figure 4C). When the bioluminescence from T^{Luc+} cells was utilized to normalize the total fluorescence in tumors, a significantly higher G-SNAT-Cy5 activation and retention were observed in CAR T^{Luc+} cells treated than activated untransduced CD8+ T^{Luc+} cells treated tumors (Figure 4D). Further *ex vivo* analysis showed that the detection of G-SNAT-Cy5 highly correlated to the expression of gzmB in semisolid tumors (Figure 4E and F), and the colocalization of CD8α, gzmB, and G-SNAT-Cy5 was confirmed by immunofluorescence staining (Figure 4G). Hence, the significant and stable detection of our G-SNAT in an acidic semi-solid tumor microenvironment after extended time periods of adoptive cell transfer provides promising features that warrant further investigation in diverse tumor murine models.

To better mimic the clinical scenario, we employed a systemically delivered lymphoma model in which A20^{Luc+} cells were intravenously injected (i.v., tail vein) into sublethally (4.4 Gy) irradiated BALB/c mice (Figure 4H). In agreement with what has been reported previously,[64] by the time of CD19-28ζ CAR T cell administration (2.4 × 10^6, i.v., retro orbital), 7 days after tumor inoculation, A20^{Luc+} cells were infiltrating the liver and lymphoid organs, including bone marrow (Figure 4I and J and Supporting Information Figure S17). Longitudinal bioluminescence imaging with D-luciferin revealed the therapeutic effect of CAR T cells. Fluorescence imaging performed 1 h post tail vein administration (i.v.) of 5 nmol G-SNAT-Cy5 at day 11 showed a significantly higher retention of the probe in the liver, spleen, and bone marrow regions of CAR T cells treated mice (Figure 4K, L). Collectively, these results suggest that G-SNAT-Cy5 detects both intracellular and exocytosed gzmB during CAR T cells mediated cancer cell killing and tumor eradication which might be useful in reporting tumor response to CAR T-cell therapy as well as trafficking of cytotoxic T cells.

Bioluminescence and G-SNAT-Cy5 Fluorescence Imaging Monitor Tumor Response to Checkpoint Blockade Therapy. To visualize the immune activation to checkpoint blockade therapy, we performed longitudinal bioluminescence and fluorescence imaging of a syngeneic mouse model treated with a combined regimen of anti-PD1 and anti-CTLA4 antibodies. As outlined in Figure 5A, transgenic Fluc+ BALB/c mice were implanted subcutaneously with 1 × 10^6 CT26 murine colorectal cancer cells and treated with 200 μg of anti-PD1 and 100 μg of anti-CTLA4 intraperitoneally at day 9, 12, and 15 postinoculation. As indicated by tumor growth curves, this combination therapy triggered a heterogeneous response (Figure 5B). We defined those treated without complete tumor regression at the end point (day 35) as nonresponders (gray) and found that the tumor sizes in responders and nonresponders diverged at day 15. All treated responder, nonresponder, and nontreated cohorts were imaged longitudinally with D-luciferin, G-SNAT-Cy5, and a previously developed gzmB specific bioluminogenic substrate GBLI2 (Supporting Information Figure S18) at day 9, 12, 15, 18, and 20. With D-luciferin, the expansion and whole-body trafficking of hematopoietic cells in response to the checkpoint blockade could be monitored. Additional GBLI2 imaging provided a reference of gzmB activity for the validation of G-SNAT-Cy5.

The baseline uptake and distribution of these probes were first evaluated with healthy Fluc+ BALB/c mice (Figure 5C). Via i.p. injection (3 mg), the bioluminescence from D-luciferin was mainly restricted to the abdomen, which is ideally suitable for imaging immune cell trafficking to the tumor site. GBLI2 imaging (200 μg, i.v. retro-orbital) gave approximately two magnitudes of weaker bioluminescence but which was highly concentrated in the spleen (Figure 5C) and to a lesser extent in the bone marrow, which suggested the major homing organs of CTLs. G-SNAT-Cy5, 1 h post i.v. injection (5 nmol, retro orbital), showed some uptake in the upper abdomen, in contrast to fast clearance of Cy5 fluorophore alone (5 nmol, i.v. retro orbital) (Figure 5C). Further dissection and organ imaging revealed that the uptake of G-SNAT-Cy5 was mainly associated with the gastrointestinal tract (Supporting Information Figure S19). Next, we imaged tumor-implanted mice receiving checkpoint blockade therapy. Consistent with growth curves, bright-field imaging showed divergent tumor responses to the checkpoint blockade (Figure 5D and Supporting Information Figure S20). Responders showed an increase in tumor volume initially at day 12, 3 days post the first treatment, and then a sustained shrinkage from day 15 to 20. Nontreated mice and treated nonresponders had continuous tumor growth. When imaged with D-luciferin, an activation of immune cells was seen in treated cohorts at day 12, indicated by enhanced bioluminescence surrounding tumors. GBLI2 imaging showed the activation of CTLs in all three cohorts regardless of treatment, but only the treated responders had obvious infiltration and gzmB activity in the tumors. Through longitudinal imaging, a distinct, ringlike pattern which might represent gradual immune cell exclusion from tumors was observed in nonresponder and nontreated cohorts. Such a ring pattern, however, was not observed in responders through the course of treatment (day 12−20). Compared to D-luciferin and GBLI2, G-SNAT-Cy5 imaging revealed an overall similar distribution but afforded a greater confined fluorescence signal and improved contrast within the tumor (Figure 5D).

To quantify the dynamic change of and compare the bioluminescent and fluorescent signals in different cohorts, we defined ROIs on tumors and calculated the relative percent difference using the treated nonresponders as the reference (Figure 5E−G and Supporting Information Figure S21). By tracking total immune cells with D-luciferin, an elevated tumor infiltration was observed since day 12, and the infiltrates were maintained through the whole process of tumor eradication in responders. GBLI2 and G-SNAT-Cy5 correlated well to immune cell infiltration in responders since day 12 which predicted the therapeutic outcome prior to tumor volume divergence. Follow-up mouse and tumor imaging at day 16 confirmed a higher G-SNAT-Cy5 in responders (Figure 5H and I) which correlated to the level of gzmB expression (Figure 5J) and localization (Figure 5K and Supporting Information Figure S22). Taken together, by visualizing the dynamics of immune cell trafficking and gzmB-mediated cytotoxicity, we observed the essential role of early and sustained CTLs infiltration in battling solid tumors. G-SNAT-Cy5 gzmB imaging could reliably differentiate and predict tumor response to checkpoint blockade therapy earlier than conventional imaging of tumor burden.

■ DISCUSSION

Conventional immune profiling offers single-cell and molecular analysis of biopsy samples but has many known limitations such as invasive nature and lack of longitudinal information.[15] Molecular imaging has yielded different strategies to noninvasively monitor tumor response to immunotherapies such as the immunoPET strategy that combines the specificity of monoclonal antibodies and inherent sensitivity of PET to detect immune cell population, expression, and distribution of target antigens. Nonetheless, several gaps remain with immunoPET: (1) Membrane associated immune markers are often expressed by more than one cell population. For instance, CD8 has been mainly identified on CTLs but could also be found on regulatory T cells, NK cells, and dendritic cells,[65,66] all of which could be present in the tumor microenvironment at an early stage.[67] (2) The mere presence of immune cells may not represent their functions. (3) Expression of immune targets may not fully correlate to therapeutic response such as PD-L1.[68] (4) Antibody-based imaging probes usually have poor tissue/tumor penetration and a long circulation half-life (days to weeks), which necessitates long half-life radioisotopes associated with high radiation exposure.[69] New strategies, especially functional imaging at the cell level, are thus needed to fill the gaps for noninvasive imaging of immune activity.

One of the alternative approaches is to image the activity of gzmB, a key enzyme involved in the granule-mediated cytotoxicity by NK cells and CTLs. Based on the versatile TESLA strategy, we first developed G-SNAT for imaging the activity of gzmB in mouse models of CAR T-cell and checkpoint blockade therapies. In comparison to other gzmB-imaging probes, G-SNAT was initially administered in a format of small molecule and was converted by active gzmB *in situ* to nanoparticles. In this work, we proved the fluorescence imaging by labeling G-SNAT with a near-infrared dye Cy5. As demonstrated in multimodality imaging of caspase-3 and methionine aminopeptidase II activity,[45−49] the modular design of the TESLA strategy should allow us to label G-SNAT with a positron-emitting isotope like ^{18}F for translational PET imaging that will overcome the limited tissue penetration with fluorescence imaging.

GzmB is produced in the cytosol as a zymogen with an N-terminal Gly-Glu dipeptide that inhibits the assembly of a functional catalytic triad.[59] In the Golgi, pro-gzmB is tagged with a mannose 6-phosphate for targeting the granules[70] where dipeptidyl peptidase I (DPPI, cathepsin C) cleaves the Gly-Glu dipeptide to generate active gzmB.[71] The active enzyme is then deposited on a scaffold of serglycin[72,73] under acidic conditions (∼pH 5.5).[74,75] It is believed that these mechanisms tightly regulate gzmB function within effector lymphocytes prior to being released from granules.[32,33] However, there are also reports that gzmB remained partially active in granules and turned on fluorogenic small[76] or cell permeable macromolecules.[35] Our results showed that gzmB could process G-SNAT-Cy5 in a buffer system at ∼ pH 5.5 and maintain ∼25% of its activity at the optimal pH 7.4 (Figure 3C and Supporting Information Figure S8), consistent with an early study.[77] Taking into account that granule-released, serglycin-bound gzmB could trigger apoptosis of target cells as efficient as free enzymes,[78] we believe the activation and retention of G-SNAT-Cy5 within CTLs are dependent on the gzmB activity. The different observations of gzmB activity in CTLs may be explained by the varied permeability of probes to cell or granule membranes. The unique property of G-SNAT-Cy5 allowed it to detect the remaining gzmB activity in CTLs. We observed no impact of G-SNAT-Cy5 labeling on the granule releasing and cytotoxic killing (Figure 3D). Our previous work has shown that the *in vivo* assembled nanoaggregates were cleared from the target site with a half-life of 244 min.[48] It is thus attempting to evaluate if G-SNAT can be applied to label and track CTLs *in vivo*. This new feature represents another advantage of our TESLA-based granzyme B probes.

To date, five CAR T-cell therapies have been approved by the FDA to treat several types of lymphomas and leukemias, as well as multiple myeloma. Despite great success in hematological malignancies, harnessing CAR T cells for treating solid tumors has seen little progress. Current research focuses on improving tumor infiltration, persistence, and potency in heterogeneous and immunosuppressive tumor microenvironments.[79] As demonstrated in our preclinical lymphoma tumor models, G-SNAT gzmB imaging in combination with bioluminescence imaging may facilitate these efforts by reporting the distribution of CAR T cells and the onset of cytotoxic killing. In the subcutaneously implanted, semisolid lymphoid tumors, bioluminescence imaging indicated more activated, untransduced CD8+ T cells than CAR T cells post intratumoral injection; on the other hand, G-SNAT gzmB imaging showed more activity from CAR T cells. This example demonstrated the value of sequential imaging of multiple targets in the same tumors in reporting the complex immune activity. Bioluminescence imaging also revealed a decrease of CAR T cell viability post

https://doi.org/10.1021/acscentsci.2c00142
ACS Cent. Sci. 2022, 8, 590−602

intratumoral injection (Figure 4B and Supporting Information Figure S15). This decay might reflect the gradual exhaustion or senescence of CAR T cells overwhelmed by CD19 antigens within the tumor microenvironment. A20 lymphoma cells were known to express high levels of PD-L1, and a combined treatment of anti-PD-L1 antibody and ibrutinib, an approved Bruton's tyrosine kinase inhibitor, could cure established A20 tumors.[80] It is worthwhile to investigate in the future how these CAR T cells lost persistence within the semisolid A20 tumors and whether a checkpoint inhibitor could reverse that. It will also be interesting to examine if G-SNAT gzmB imaging could be utilized to differentiate malfunctioning CAR T cells *in vivo* since cumulative data have suggested that senescent T cells have a reduced expression of gzmB[81] and exhausted CTLs have impaired granzyme packaging and degranulation[82,83] and thus a defect in gzmB release and cytotoxicity. The modular design of the TESLA strategy allows G-SNAT to be readily engineered by replacing the mouse gzmB peptide substrate with the sequence preferred by human gzmB. It should enable the detection of human CAR T cell mediated cytotoxicity in treating human cancer xenografts in mouse models and potentially in clinical trials.

While checkpoint inhibitors have been adopted to treat a variety of solid tumor types, only a small percentage of patients exhibit complete response, and early detection of antitumor immunity remains challenging. By imaging CT26 colorectal tumors whose responses to anti-PD-1/anti-CTLA4 were dichotomous, we found that checkpoint blockade therapy cured cancer by stimulating and maintaining early immune cell infiltration including activated and expanded CTLs, which led to gradually intensified cytotoxicity at the tumor site that was inversely proportional to the tumor volume (Figure 5). These findings are consistent with a previous immune profiling by flow cytometry and gene expression analysis showing that responded CT26 tumors contained expanded T and NK cell populations with CD8+ T cells that nearly doubled 3 days after the third round of anti-PD-1/anti-CTLA-4 treatment.[84] At this point, G-SNAT or GBLI2 imaging was not able to differentiate gzmB activity from NK and certain gzmB expressing regulatory T cells or between newly infiltrated and tumor-surrounding effector lymphocytes, but unlike conventional immune profiling, G-SNAT gzmB imaging would advance spatially and temporally correlated surveillance of cytotoxicity and predict tumor early response *in vivo*. Our longitudinal imaging revealed a distinct ring pattern surrounding the tumors or so-called "immune dessert" in both advanced untreated and treated nonresponding tumors. With current imaging, we could not rule out the possibility that the rings were formed due to lack of tumor-infiltrated immune cells or CTLs gradually losing their viability. But a similar pattern displayed by longitudinal immunoPET with an ^{89}Zr-labeled PEGylated variable region segment of camelid heavy chain-only antibody targeting CD8 from Rashidian et al.[18] supported our conclusion that CTLs were exiled from advanced tumors. Future combination of G-SNAT functional imaging and cell tracking immunoPET should sketch a more comprehensive picture of how the immune system interacts with tumor cells upon checkpoint blockade therapy and may generate new insights leading to the development of more potent therapies.

In conclusion, we developed a novel gzmB-activated self-assembly imaging probe and proved conceptually that G-SNAT-Cy5 fluorescence imaging could be utilized to monitor cytotoxic activity and predict tumor response to CAR T-cell and checkpoint blockade therapies. Together with longitudinally whole-body bioluminescence imaging, the trafficking and tumor infiltration of total splenocytes or CTLs in responding to immunotherapies were visualized, which revealed an essential role of early immune infiltration and persistent cytotoxic activity in curing cancer. These results support further development of G-SNAT for PET imaging of the immune response in patients and also highlight the value of multiparameter imaging for studying the cytotoxic function in the context of immune cell interplay, tumor microenvironments, and new cancer immunotherapy.

■ ASSOCIATED CONTENT

Supporting Information

The Supporting Information is available free of charge at https://pubs.acs.org/doi/10.1021/acscentsci.2c00142.

- Materials and Methods; supplementary Figures S1−S22 as described in the text showing synthesis, imaging, analysis, and spectra; Appendix of NMR spectra (PDF)
- Imaging of G-SNAT-Cy5 nanoaggregates in a single naive CD8+ T cell (AVI)
- Imaging of G-SNAT-Cy5 nanoaggregates in a single activated untransduced CD8+ T cell (AVI)
- Imaging of G-SNAT-Cy5 nanoaggregates in a single CD19-28ζ CAR T cell (AVI)

■ AUTHOR INFORMATION

Corresponding Author

Jianghong Rao − *Department of Radiology, Molecular Imaging Program at Stanford, Stanford University School of Medicine, Stanford, California 94305, United States; Department of Chemistry, Stanford University, Stanford, California 94305, United States;* orcid.org/0000-0002-5143-9529; Email: jrao@stanford.edu

Authors

Jinghang Xie − *Department of Radiology, Molecular Imaging Program at Stanford, Stanford University School of Medicine, Stanford, California 94305, United States*

Fadi El Rami − *Department of Radiology, Molecular Imaging Program at Stanford, Stanford University School of Medicine, Stanford, California 94305, United States*

Kaixiang Zhou − *Department of Radiology, Molecular Imaging Program at Stanford, Stanford University School of Medicine, Stanford, California 94305, United States*

Federico Simonetta − *Division of Blood and Marrow Transplantation, Department of Medicine, Stanford University Medical Center, Stanford, California 94305, United States*

Zixin Chen − *Department of Chemistry, Stanford University, Stanford, California 94305, United States*

Xianchuang Zheng − *Department of Radiology, Molecular Imaging Program at Stanford, Stanford University School of Medicine, Stanford, California 94305, United States*

Min Chen − *Department of Radiology, Molecular Imaging Program at Stanford, Stanford University School of Medicine, Stanford, California 94305, United States;* orcid.org/0000-0002-6488-455X

Preethi B. Balakrishnan − *Department of Radiology, Molecular Imaging Program at Stanford, Stanford University School of Medicine, Stanford, California 94305, United States*

https://doi.org/10.1021/acscentsci.2c00142
ACS Cent. Sci. 2022, 8, 590−602

Sheng-Yao Dai − *Department of Radiology, Molecular Imaging Program at Stanford, Stanford University School of Medicine, Stanford, California 94305, United States*

Surya Murty − *Department of Radiology, Molecular Imaging Program at Stanford, Stanford University School of Medicine, Stanford, California 94305, United States; Department of Bioengineering, Stanford University, Stanford, California 94305, United States*

Israt S. Alam − *Department of Radiology, Molecular Imaging Program at Stanford, Stanford University School of Medicine, Stanford, California 94305, United States*

Jeanette Baker − *Division of Blood and Marrow Transplantation, Department of Medicine, Stanford University Medical Center, Stanford, California 94305, United States*

Robert S. Negrin − *Division of Blood and Marrow Transplantation, Department of Medicine, Stanford University Medical Center, Stanford, California 94305, United States*

Sanjiv S. Gambhir − *Department of Radiology, Molecular Imaging Program at Stanford, Stanford University School of Medicine, Stanford, California 94305, United States; Department of Bioengineering and Department of Materials Science & Engineering, Stanford University, Stanford, California 94305, United States;* orcid.org/0000-0002-2711-7554

Complete contact information is available at:
https://pubs.acs.org/10.1021/acscentsci.2c00142

Author Contributions

J.X., F.E.R., and J.R. designed and led the study. K.Z., Z.C., S.-Y.D., and J.X. performed the probe synthesis and analysis. X.Z. performed TEM and DLS studies. F.E.R., S.M. and J.X. generated naive, activated untransduced CD8+ and CAR T cells. J.X. performed confocal imaging. F.S., F.E.R., and J.X. generated and imaged the CAR T cell therapy mouse models. M.C., P.B.B., and J.X. generated and imaged the checkpoint blockade therapy mouse model. P.B.B. performed immunofluorescence staining. F.S., I.S.A., J.B., R.S.N., and S.S.G. contributed to the design and data analysis of CAR T cell therapy models. J.B., F.S., and R.S.N. provided transgenic and Rag2$^{-/-}\gamma$c$^{-/-}$ mice for the study. J.X., F.E.R., and J.R. analyzed all the data and wrote the manuscript with inputs from all coauthors.

Author Contributions

□These authors contributed equally to this work.

Notes

The authors declare the following competing financial interest(s): J.X., Z.C., M.C., and J.R. are inventors on a U.S. patent application submitted by Leland Junior Stanford University that covers some of this work. All other authors declare that they have no competing interests.

All data associated with this study are present in the paper or Supporting Information. Materials are available and will be provided under the material transfer policies of Stanford University. These requests should be directed to the corresponding author.

■ ACKNOWLEDGMENTS

We thank the Stanford Neuroscience Microscopy Service (NMS) (supported by NIH NS069375) for help with confocal imaging, the Stanford Shared FACS Facility for instrumentation and assistance with flow cytometry, the Functional Genomics Facility at Stanford for access to LI-COR Odyssey for western blots, and the Stanford Center for Innovation in In-Vivo Imaging (SCI^3) for instrumentation and assistance with animal imaging. This work was supported by NIH grants U54CA199075 (Center for Cancer Nanotechnology Excellence for Translational Diagnostics, CCNE-TD), R01CA199656, and R01CA201719 (S.S.G.). J.X. thanks the Molecular Imaging Program at Stanford for the Molecular Imaging Young Investigator (MIYI) Prize. M.C. acknowledges the support from the Stanford Cancer Translational Nanotechnology Training Program funded by NCI award T32CA196585.

■ REFERENCES

(1) Khalil, D. N.; Smith, E. L.; Brentjens, R. J.; Wolchok, J. D. The future of cancer treatment: immunomodulation, CARs and combination immunotherapy. *Nat. Rev. Clin Oncol* **2016**, *13*, 273−290.

(2) Kruger, S.; et al. Advances in cancer immunotherapy 2019 - latest trends. *J. Exp Clin Cancer Res.* **2019**, *38*, 268.

(3) Ramachandran, I.; et al. Systemic and local immunity following adoptive transfer of NY-ESO-1 SPEAR T cells in synovial sarcoma. *J. Immunother Cancer* **2019**, *7*, 276.

(4) Ando, M.; Ito, M.; Srirat, T.; Kondo, T.; Yoshimura, A. Memory T cell, exhaustion, and tumor immunity. *Immunol Med.* **2020**, *43*, 1−9.

(5) Cohen, A. D.; et al. How to train your T cells: Overcoming immune dysfunction in multiple myeloma. *Clin. Cancer Res.* **2020**, *26*, 1541−1554.

(6) Lei, X.; et al. Immune cells within the tumor microenvironment: Biological functions and roles in cancer immunotherapy. *Cancer Lett.* **2020**, *470*, 126−133.

(7) Minton, K. Overcoming CAR T cell exhaustion. *Nat. Rev. Immunol* **2020**, *20*, 72−73.

(8) Martinez, M.; Moon, E. K. CAR T Ccells for solid tumors: New strategies for finding, infiltrating, and surviving in the tumor mcroenvironment. *Front Immunol* **2019**, *10*, 128.

(9) Labanieh, L.; Majzner, R. G.; Mackall, C. L. Programming CAR-T cells to kill cancer. *Nat. Biomed Eng.* **2018**, *2*, 377−391.

(10) Peeters, M. J. W.; Rahbech, A.; Thor Straten, P. TAM-ing T cells in the tumor microenvironment: implications for TAM receptor targeting. *Cancer Immunol Immunother* **2020**, *69*, 237−244.

(11) Wang, R.; et al. Blocking migration of regulatory T cells to leukemic hematopoietic microenvironment delays disease progression in mouse leukemia model. *Cancer Lett.* **2020**, *469*, 151−161.

(12) Fraietta, J. A.; et al. Determinants of response and resistance to CD19 chimeric antigen receptor (CAR) T cell therapy of chronic lymphocytic leukemia. *Nat. Med.* **2018**, *24*, 563−571.

(13) Walker, A. J.; et al. Tumor antigen and receptor densities regulate efficacy of a chimeric antigen receptor targeting anaplastic lymphoma kinase. *Mol. Ther* **2017**, *25*, 2189−2201.

(14) Haslam, A.; Prasad, V. Estimation of the percentage of US patients with cancer who are eligible for and respond to checkpoint inhibitor immunotherapy drugs. *JAMA Netw Open* **2019**, *2*, e192535.

(15) McCarthy, C. E.; White, J. M.; Viola, N. T.; Gibson, H. M. In vivo imaging technologies to monitor the immune system. *Front Immunol* **2020**, *11*, 1067.

(16) Mall, S.; et al. Immuno-PET imaging of engineered human T cells in tumors. *Cancer Res.* **2016**, *76*, 4113−4123.

(17) Tavaré, R.; et al. An Effective immuno-PET imaging method to monitor CD8-dependent responses to immunotherapy. *Cancer Res.* **2016**, *76*, 73−82.

(18) Rashidian, M.; et al. Predicting the response to CTLA-4 blockade by longitudinal noninvasive monitoring of CD8 T cells. *J. Exp Med.* **2017**, *214*, 2243−2255.

(19) Alam, I. S.; et al. Visualization of activated T cells by OX40-ImmunoPET as a strategy for diagnosis of acute graft-versus-host disease. *Cancer Res.* **2020**, *80*, 4780−4790.
(20) Natarajan, A.; et al. A novel engineered small protein for Positron Emission Tomography imaging of human programmed death ligand-1: Validation in mouse models and human cancer tissues. *Clin. Cancer Res.* **2019**, *25*, 1774−1785.
(21) Ronald, J. A.; et al. A PET imaging strategy to visualize activated T cells in acute graft-versus-host disease elicited by allogenic hematopoietic cell transplant. *Cancer Res.* **2017**, *77*, 2893−2902.
(22) Levi, J.; et al. Imaging of activated T cells as an early predictor of immune response to anti-PD-1 therapy. *Cancer Res.* **2019**, *79*, 3455−3465.
(23) Sato, E.; et al. Intraepithelial CD8+ tumor-infiltrating lymphocytes and a high CD8+/regulatory T cell ratio are associated with favorable prognosis in ovarian cancer. *Proc. Natl. Acad. Sci. U. S. A.* **2005**, *102*, 18538−18543.
(24) Kawai, O.; et al. Predominant infiltration of macrophages and CD8(+) T Cells in cancer nests is a significant predictor of survival in stage IV nonsmall cell lung cancer. *Cancer* **2008**, *113*, 1387−1395.
(25) Yamada, N.; et al. CD8+ tumor-infiltrating lymphocytes predict favorable prognosis in malignant pleural mesothelioma after resection. *Cancer Immunol Immunother* **2010**, *59*, 1543−1549.
(26) Schwartz, R. H. T cell anergy. *Annu. Rev. Immunol.* **2003**, *21*, 305−334.
(27) Roychoudhuri, R.; Eil, R. L.; Restifo, N. P. The interplay of effector and regulatory T cells in cancer. *Curr. Opin Immunol* **2015**, *33*, 101−111.
(28) Larimer, B. M.; et al. Granzyme B PET imaging as a predictive biomarker of immunotherapy response. *Cancer Res.* **2017**, *77*, 2318−2327.
(29) Scott, J. I.; et al. A functional chemiluminescent probe for in vivo imaging of natural killer cell activity against tumours. *Angew. Chem., Int. Ed. Engl.* **2021**, *60*, 5699−5703.
(30) Cullen, S. P.; Martin, S. J. Mechanisms of granule-dependent killing. *Cell Death Differ.* **2008**, *15*, 251−262.
(31) Doß, B. T. M. *Generation of an expression system for human granzyme B and analysis of the in vitro and in vivo efficiency*. Doctoral Dissertation, Ludwig Maximilian University of Munich, 2010.
(32) Packard, B. Z.; Telford, W. G.; Komoriya, A.; Henkart, P. A. Granzyme B activity in target cells detects attack by cytotoxic lymphocytes. *J. Immunol* **2007**, *179*, 3812−3820.
(33) Choi, P. J.; Mitchison, T. J. Imaging burst kinetics and spatial coordination during serial killing by single natural killer cells. *Proc. Natl. Acad. Sci. U. S. A.* **2013**, *110*, 6488−6493.
(34) Konishi, M.; et al. Imaging granzyme B activity assesses immune-mediated myocarditis. *Circ. Res.* **2015**, *117*, 502−512.
(35) He, S.; Li, J.; Lyu, Y.; Huang, J.; Pu, K. Near-infrared fluorescent macromolecular reporters for real-time imaging and urinalysis of cancer immunotherapy. *J. Am. Chem. Soc.* **2020**, *142*, 7075−7082.
(36) Zhang, Y.; et al. Activatable polymeric nanoprobe for near-infrared fluorescence and photoacoustic imaging of T lymphocytes. *Angew. Chem., Int. Ed. Engl.* **2021**, *60*, 5921−5927.
(37) Zhao, N.; et al. In vivo measurement of granzyme proteolysis from activated immune cells with PET. *ACS Cent Sci.* **2021**, *7*, 1638−1649.
(38) Larimer, B. M.; et al. The effectiveness of checkpoint inhibitor combinations and administration timing can be measured by granzyme B PET imaging. *Clin. Cancer Res.* **2019**, *25*, 1196−1205.
(39) LaSalle, T.; et al. Granzyme B PET imaging of immune-mediated tumor killing as a tool for understanding immunotherapy response. *J. Immunother Cancer* **2020**, *8*, e000291.
(40) Ren, H.; et al. A biocompatible condensation reaction for labeling of N-terminal cysteine on proteins. *Angew. Chem. Int. Ed* **2009**, *48*, 9658−9662.
(41) Ye, D.; Liang, G.; Ma, M. L.; Rao, J. Controlling intracellular macrocyclization for the imaging of protease activity. *Angew. Chem. Int. Ed* **2011**, *50*, 2275−2279.
(42) Chen, Z.; et al. Exploring condensation reaction between aromatic nitriles and aminothiols to form nanoparticles in cells for imaging the activity of hydrolytic enzymes. *Angew. Chem. Int. Ed* **2020**, *59*, 3272−3279.
(43) Liang, G.; Ren, H.; Rao, J. A biocompatible condensation reaction for controlled assembly of nanoparticles in cells. *Nat. Chemistry* **2010**, *2*, 54−60.
(44) Ye, D.; et al. Bioorthogonal cyclization and *in situ* self-assembly of small-molecule probes for imaging caspase activity in living mice. *Nat. Chemistry* **2014**, *6*, 519−526.
(45) Dragulescu-Andrasi, A.; Kothapalli, S. R.; Tikhomirov, G. A.; Rao, J.; Gambhir, S. S. Activatable oligomerizable imaging agents for photoacoustic imaging of furin-like activity in living subjects. *J. Am. Chem. Soc.* **2013**, *135*, 11015−11022.
(46) Shuhendler, A. J.; et al. Molecular Magnetic Resonance Imaging of Tumor Response to Therapy. *Sci. Rep* **2015**, *5*, 14759.
(47) Xie, J.; et al. In Vivo Imaging of Methionine Aminopeptidase II for Prostate Cancer Risk Stratification. *Cancer Res.* **2021**, *81*, 2510−2521.
(48) Chen, Z.; Chen, M.; Zhou, K.; Rao, J. Pre-targeted Imaging of Protease Activity through In Situ Assembly of Nanoparticles. *Angew. Chem. Int. Ed* **2020**, *59*, 7864−7870.
(49) Chen, M.; et al. [18F]-C-SNAT4: an improved caspase-3-sensitive nanoaggregation PET tracer for imaging of tumor responses to chemo- and immunotherapies. *Eur. J. Nucl. Med. Mol. Imaging* **2021**, *48*, 3386−3399.
(50) Voskoboinik, I.; Whisstock, J. C.; Trapani, J. A. Perforin and granzymes: function, dysfunction and human pathology. *Nat. Rev. Immunol* **2015**, *15*, 388−400.
(51) Cullen, S. P.; Adrain, C.; Luthi, A. U.; Duriez, P. J.; Martin, S. J. Human and murine granzyme B exhibit divergent substrate preferences. *J. Cell Biol.* **2007**, *176*, 435−444.
(52) Trapani, J. A.; et al. Efficient nuclear targeting of granzyme B and the nuclear consequences of apoptosis induced by granzyme B and perforin are caspase-dependent, but cell death is caspase-independent. *J. Biol. Chem.* **1998**, *273*, 27934−27938.
(53) Adrain, C.; Murphy, B. M.; Martin, S. J. Molecular ordering of the caspase activation cascade initiated by the cytotoxic T lymphocyte/natural killer (CTL/NK) protease granzyme B. *J. Biol. Chem.* **2005**, *280*, 4663−4673.
(54) Metkar, S. S.; et al. Cytotoxic cell granule-mediated apoptosis: perforin delivers granzyme B-serglycin complexes into target cells without plasma membrane pore formation. *Immunity* **2002**, *16*, 417−428.
(55) Thiery, J.; et al. Perforin pores in the endosomal membrane trigger the release of endocytosed granzyme B into the cytosol of target cells. *Nat. Immunol* **2011**, *12*, 770−777.
(56) Casciola-Rosen, L.; et al. Mouse and human granzyme B have distinct tetrapeptide specificities and abilities to recruit the bid pathway. *J. Biol. Chem.* **2007**, *282*, 4545−4552.
(57) Andrade, F.; et al. Granzyme B directly and efficiently cleaves several downstream caspase substrates: implications for CTL-induced apoptosis. *Immunity* **1998**, *8*, 451−460.
(58) Lee, J.; Sadelain, M.; Brentjens, R. Retroviral transduction of murine primary T lymphocytes. *Methods Mol. Biol.* **2009**, *506*, 83−96.
(59) Caputo, A.; Garner, R. S.; Winkler, U.; Hudig, D.; Bleackley, R. C. Activation of recombinant murine cytotoxic cell proteinase-1 requires deletion of an amino-terminal dipeptide. *J. Biol. Chem.* **1993**, *268*, 17672−17675.
(60) Davenport, A. J.; et al. Chimeric antigen receptor T cells form nonclassical and potent immune synapses driving rapid cytotoxicity. *Proc. Natl. Acad. Sci. U. S. A.* **2018**, *115*, E2068−E2076.
(61) Mount, C. W.; et al. Potent antitumor efficacy of anti-GD2 CAR T cells in H3-K27M(+) diffuse midline gliomas. *Nat. Med.* **2018**, *24*, 572−579.
(62) Gao, C. F.; et al. Caspase-dependent cytosolic release of cytochrome c and membrane translocation of Bax in p53-induced apoptosis. *Exp. Cell Res.* **2001**, *265*, 145−151.

https://doi.org/10.1021/acscentsci.2c00142
ACS Cent. Sci. 2022, 8, 590−602

(63) Beilhack, A.; et al. In vivo analyses of early events in acute graft-versus-host disease reveal sequential infiltration of T-cell subsets. *Blood* **2005**, *106*, 1113−1122.

(64) Edinger, M.; et al. Revealing lymphoma growth and the efficacy of immune cell therapies using in vivo bioluminescence imaging. *Blood* **2003**, *101*, 640−648.

(65) Baume, D. M.; Caligiuri, M. A.; Manley, T. J.; Daley, J. F.; Ritz, J. Differential expression of CD8 alpha and CD8 beta associated with MHC-restricted and non-MHC-restricted cytolytic effector cells. *Cell Immunol* **1990**, *131*, 352−365.

(66) Shortman, K.; Heath, W. R. The CD8+ dendritic cell subset. *Immunol Rev.* **2010**, *234*, 18−31.

(67) Gajewski, T. F.; Schreiber, H.; Fu, Y. X. Innate and adaptive immune cells in the tumor microenvironment. *Nat. Immunol* **2013**, *14*, 1014−1022.

(68) Herbst, R. S.; et al. Pembrolizumab versus docetaxel for previously treated, PD-L1-positive, advanced non-small-cell lung cancer (KEYNOTE-010): a randomised controlled trial. *Lancet* **2016**, *387*, 1540−1550.

(69) Maute, R. L.; et al. Engineering high-affinity PD-1 variants for optimized immunotherapy and immuno-PET imaging. *Proc. Natl. Acad. Sci. U. S. A.* **2015**, *112*, E6506−6514.

(70) Griffiths, G. M.; Isaaz, S. Granzymes A and B are targeted to the lytic granules of lymphocytes by the mannose-6-phosphate receptor. *J. Cell Biol.* **1993**, *120*, 885−896.

(71) McGuire, M. J.; Lipsky, P. E.; Thiele, D. L. Generation of active myeloid and lymphoid granule serine proteases requires processing by the granule thiol protease dipeptidyl peptidase I. *J. Biol. Chem.* **1993**, *268*, 2458−2467.

(72) Galvin, J. P.; et al. Apoptosis induced by granzyme B-glycosaminoglycan complexes: Implications for granule-mediated apoptosis in vivo. *J. Immunol.* **1999**, *162*, 5345−5350.

(73) Grujic, M.; et al. Serglycin-deficient cytotoxic T lymphocytes display defective secretory granule maturation and granzyme B storage. *J. Biol. Chem.* **2005**, *280*, 33411−33418.

(74) Burkhardt, J. K.; Hester, S.; Lapham, C. K.; Argon, Y. The lytic granules of natural killer cells are dual-function organelles combining secretory and pre-lysosomal compartments. *J. Cell Biol.* **1990**, *111*, 2327−2340.

(75) Masson, D.; Peters, P. J.; Geuze, H. J.; Borst, J.; Tschopp, J. Interaction of chondroitin sulfate with perforin and granzymes of cytolytic T-cells is dependent on pH. *Biochemistry* **1990**, *29*, 11229−11235.

(76) Janiszewski, T.; et al. Noninvasive optical detection of granzyme B from natural killer cells with enzyme-activated fluorogenic probes. *J. Biol. Chem.* **2020**, *295*, 9567−9582.

(77) Poe, M.; et al. Human cytotoxic lymphocyte granzyme B. Its purification from granules and the characterization of substrate and inhibitor specificity. *J. Biol. Chem.* **1991**, *266*, 98−103.

(78) Veugelers, K.; et al. Granule-mediated killing by granzyme B and perforin requires a mannose 6-phosphate receptor and is augmented by cell surface heparan sulfate. *Mol. Biol. Cell* **2006**, *17*, 623−633.

(79) Petty, A. J.; Heyman, B.; Yang, Y. Chimeric antigen receptor celltherapy: Overcoming obstacles to battle cancer. *Cancers* **2020**, *12*, 842.

(80) Sagiv-Barfi, I.; et al. Therapeutic antitumor immunity by checkpoint blockade is enhanced by ibrutinib, an inhibitor of both BTK and ITK. *Proc. Natl. Acad. Sci. U. S. A.* **2015**, *112*, E966−972.

(81) Yang, O. O.; et al. Decreased perforin and granzyme B expression in senescent HIV-1-specific cytotoxic T lymphocytes. *Virology* **2005**, *332*, 16−19.

(82) Riches, J. C.; et al. T cells from CLL patients exhibit features of T-cell exhaustion but retain capacity for cytokine production. *Blood* **2013**, *121*, 1612−1621.

(83) Wu, X.; et al. PD-1(+) CD8(+) T cells are exhausted in tumours and functional in draining lymph nodes of colorectal cancer patients. *Br. J. Cancer* **2014**, *111*, 1391−1399.

(84) Taylor, M. A.; et al. Longitudinal immune characterization of syngeneic tumor models to enable model selection for immune oncology drug discovery. *J. Immunother Cancer* **2019**, *7*, 328.